Supporting information: CMIP6 models validation and Amazon carbon cycle projections

Matteo Mastropierro[1], Daniele Peano[2], Davide Zanchettin[1]

[1] Department of Environmental Sciences, Statistics and informatics, Ca' Foscari University of Venice, Venice, Italy
[2] Fondazione Centro euro-Mediterraneo sui Cambiamenti Climatici, CMCC, Bologna, Italy

Correspondence to: Matteo Mastropierro (matteo.mastropierro@unive.it)

Table 1: Overview of ESMs considered in this study

ESM	Reference	Curvilinear Ocean Grid	Land carbon	Nitrogen cycle	Phosphorous cycle	Fires	Dynamic vegetation	ECS (°C)
IPSL-CM6A-LR	**(Boucher *et al.*, 2020)**	Yes	ORCHIDEE, br.2.0	No	No	No	No	4.70
CNRM-ESM2-1	**(Séférian *et al.*, 2019)**	Yes	ISBA-CTRIP	Implicit	No	Yes (natural)	No	4.79
CanESM5	**(Swart *et al.*, 2019)**	Yes	CLASS-CTEM	Implicit	No	No	dynamic wetlands	5.64
UKESM1-0-LL	**(Sellar *et al.*, 2019)**	No	JULES-ES-1.0	Yes	No	No	Yes	5.36
MIROC-ES2L	**(Hajima *et al.*, 2020)**	No	VISIT-e	Yes	No	No	No	2.66
ACCESS-ESM1-5	**(Ziehn *et al.*, 2020)**	No	CABLE	Yes	Yes	No	No	3.88
BCC-CSM2-1	**(Wu *et al.*, 2019)**	No	BCC-AVIM2	Implicit	No	Yes (natural)	No	3.02
E3SM-1-1-ECA	**(Burrows *et al.*, 2020)**	No	ELMv1.1	No	No	No	dynamic wetlands	5.31
MPI-ESM1-2-LR	**(Mauritsen *et al.*, 2019)**	Yes	JSBACH3.2	Yes	No	No	Yes	3.03
NorESM2-MM	**(Seland *et al.*, 2020)**	No	CLM5	Yes	No	Yes	No	2.49
TaiESM1	**(Wang *et al.*, 2021)**	No	CLM4	No	No	No	No	4.36
CMCC-ESM2	**(Lovato *et al.*, 2022)**	Yes	CLM-4.5	Yes	No	Yes (natural)	No	3.58
CESM2-WACCM	**(Danabasoglu *et al.*, 2020)**	No	CLM5	Yes	No	Yes	dynamic wetlands	4.68

Earth System Models evaluation

The ESM ability to simulate ENSO is first assessed in terms of the Nino3.4 index seasonality (phase-locking, Figure S1). Figure S1 clearly shows that all the models, with the exception of MPI-ESM1-2-LR, CanESM5 ACCESS-ESM1-5 and BCC-CSM2-MR, exhibit a stronger interannual variability than observations, represented by the HadISST dataset (Rayner *et al.*, 2003), during all the calendar months (black line). Those four models, on the opposite, are characterized by a lower seasonality of the ENSO signal, with higher and lower than observed variability during boreal summer and boreal winter months, respectively. Beyond the bias in the annual standard deviation, the normalized index indicates that ESMs typically yield a much higher minimum from March to August and lower maximum from September to January compared to observations (Figure S1b), thus displaying a negative bias in the amplitude of ENSO seasonal variations.

We also considered the ability of the ESMs to simulate the climatology of the Amazon basin as well as its land carbon and surface energy fluxes by assessing their seasonality. A dry precipitation bias is persistent during the whole year and for all the ESMs (Ortega *et al.*, 2021; Monteverde *et al.*, 2022, Figure S2, panel a). Despite this, however, not all the models display a consistent dry bias for soil moisture, but rather roughly half of them overestimate the volumetric soil content of water, most likely a direct consequence of the parameterization of soil water depth in the different land models used (Qiao *et al.*, 2022, Figure S2, panel c). Temperatures are also overestimated in the Amazon basin, both concerning their seasonal amplitude cycle, which is accentuated in ESM, as well as considering annual mean values. This mainly occurs during the second half of the year, while from January until July roughly half of the ESMs simulate a lower temperature compared to ERA5 reanalysis (Figure S2, panel c). Considering the energy fluxes, shortwave incoming radiation is probably the most consistent bias observable in the region considered (Figure S3, panel b), and its presence has strongly persisted since the 5th generation of CMIP models (Wild *et al.*, 2015). Despite a correct seasonality, the values of incoming radiation are almost two times the FLUXCOM ones (Jung *et al.*, 2019): this bias is a consequence of low cloudiness within the tropical basin, and most likely it is the direct factor that generates the dry precipitation bias. Latent heat does not resemble the observed pattern, as it overestimated in all the models up to July, while in the second part of the year roughly half of the ESMs project lower values than the FLUXCOM dataset. ESMs also struggle to reproduce the seasonal cycle of GPP, TER and consequently NEP (Figure S4). Here, the general behaviour of the ESMs is a shift in the lower productivity peak towards the end of the year (Figure S4 panel a). Figure S5 shows the spatially averaged NEP, GPP and TER in the Amazon basin for the DJF season. All the models depict a clear and strong underestimation of seasonal values. Compared to the FLUXOM carbon fluxes dataset (Jung *et al.*, 2020). The NEP bias is mainly due to an overestimation of TER in the DJF season for four ESMs (E3SM-1-1-ECA, MPI-ESM1-2-LR, TaiESM1, UKESM1-0-LL, Figure S4 panel b) and c) and Figure S5), while for the rest of the models this bias is the result of a combination of both low GPP and high TER. The four models with strong DJF TER bias also present high GPP values compared to FLUXCOM and the other ESMs, indicating a particularly high vegetation (and thus Land Module) sensitivity to climatological forcings.

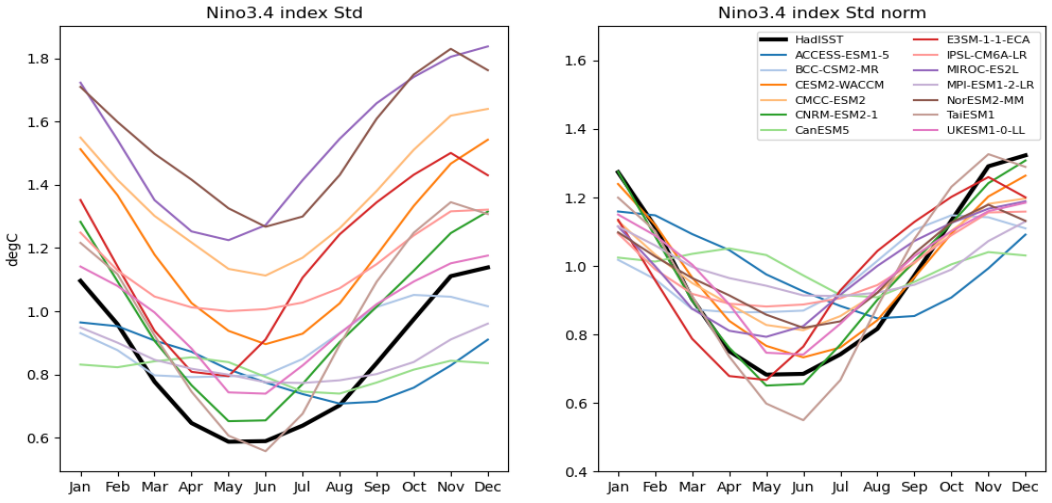

Figure S1: Model biases with respect to the HadISST dataset in ENSO seasonal variability, for the period 1979/2013. a) seasonality as expressed by the Nino3.4 index standard deviation, b) seasonality expressed by the normalized Nino3.4 standard deviation.

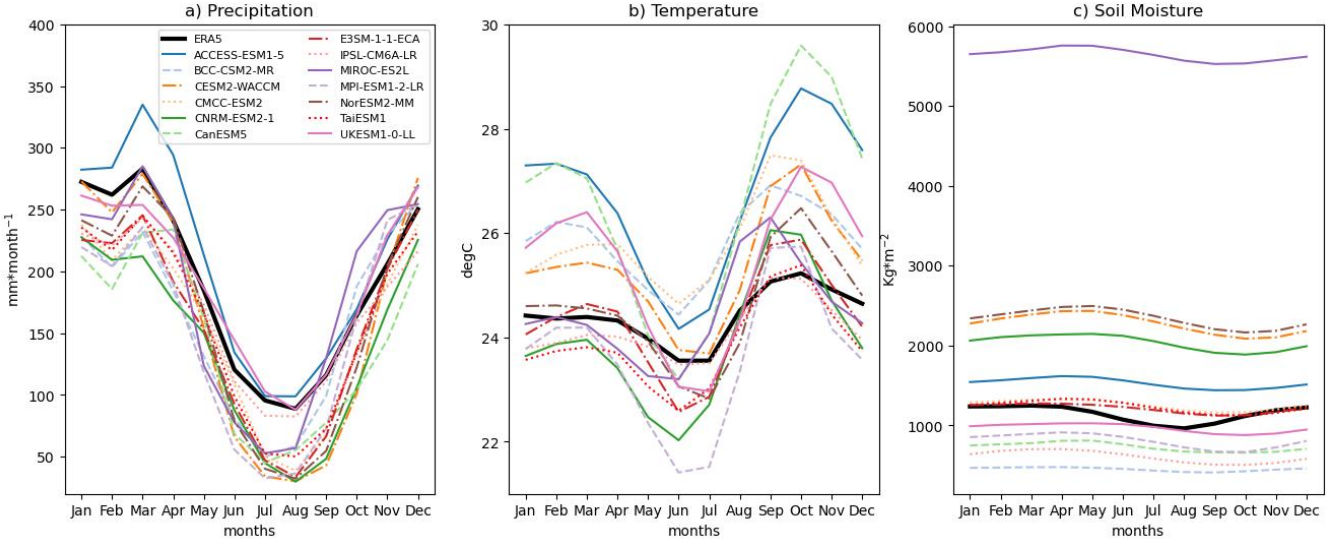

Figure S2: Model biases with respect to the ERA5 dataset in the climatological seasonal variability, for the period 1979/2013. Shown are the monthly zonal means within the Amazon basin for a) precipitation, b) temperature and c) soil moisture.

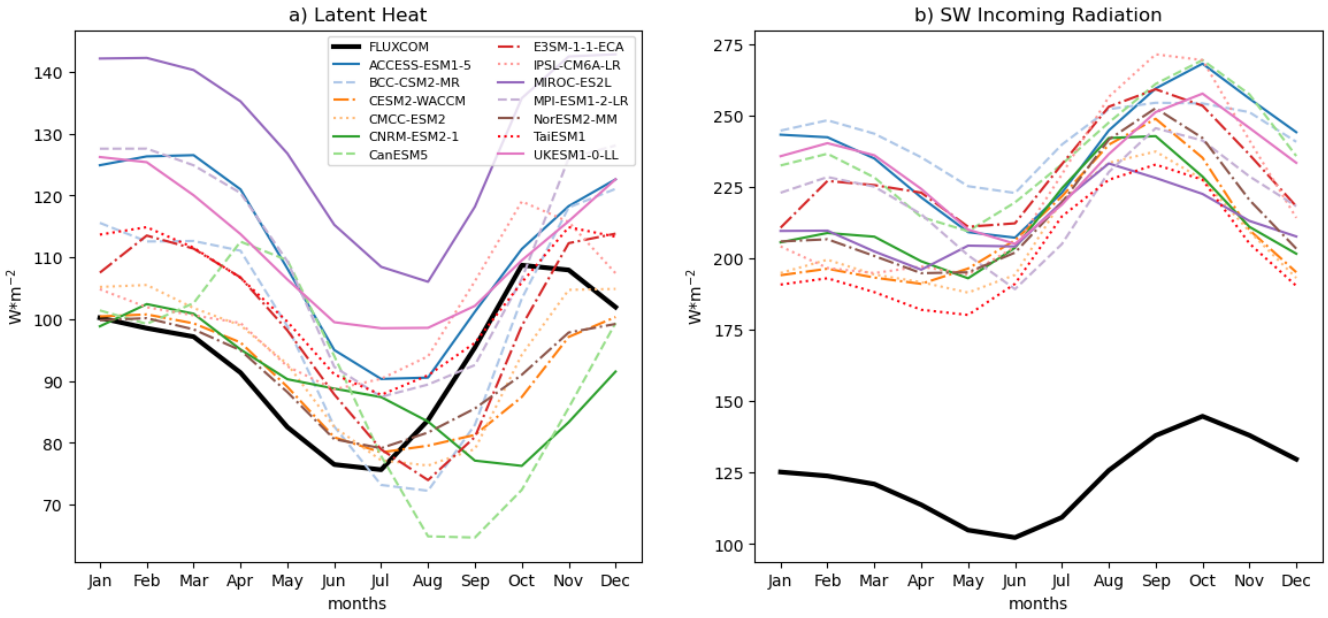

55 **Figure S3:** Model biases with respect to the FLUXCOM dataset in the seasonal variability of surface energy fluxes, for the period 1979/2013. Shown are the monthly zonal means within the Amazon basin for a) latent heat and b) shortwave incoming radiation.

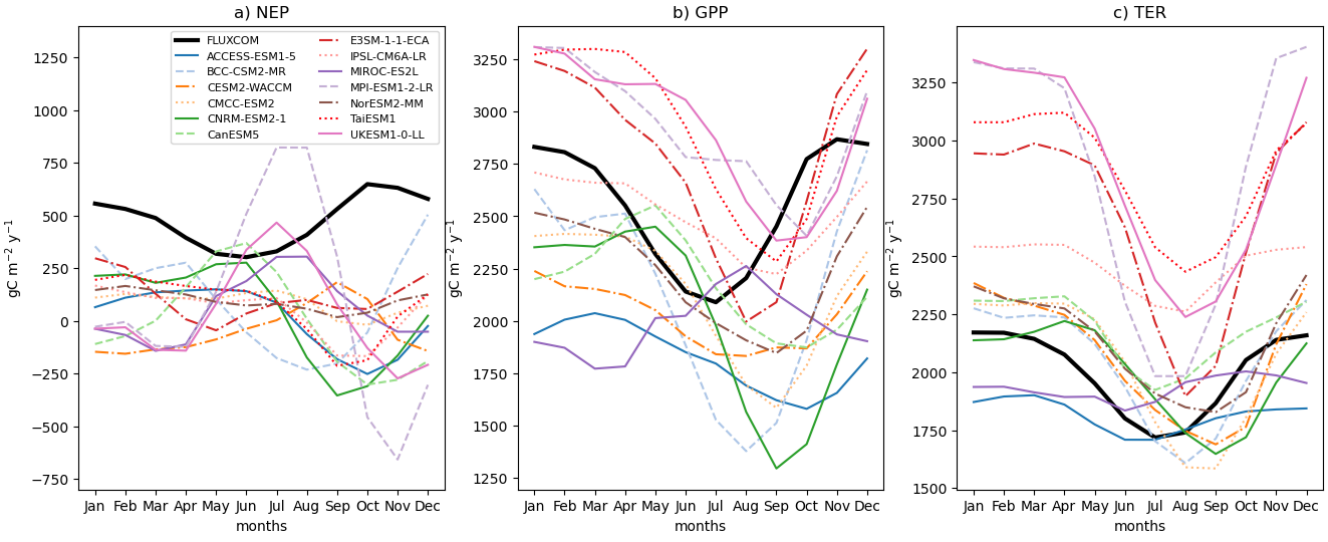

Figure S4: Model biases with respect to the FLUXCOM dataset in the seasonal variability of carbon fluxes, for the period 1979/2013.
60 Shown are the monthly zonal means within the Amazon basin for a) NEP, b) GPP and c) TER.

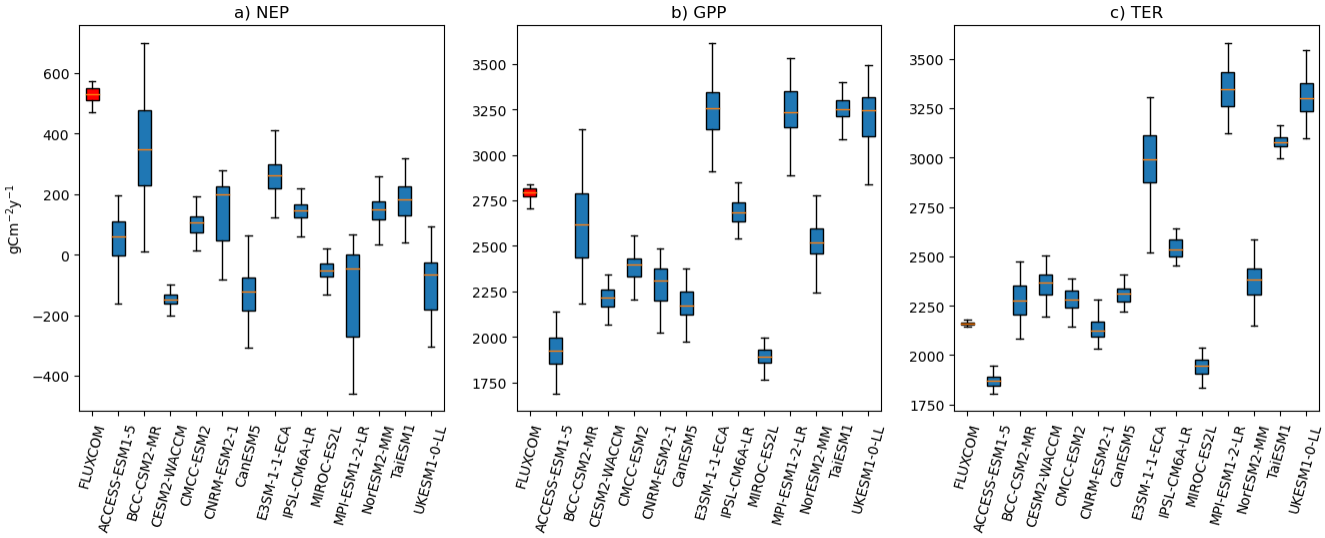

Figure S5: Model biases with respect to the FLUXCOM dataset in the DJF distribution of carbon fluxes values, for the period 1979/2013. Shown are the DJF zonal means within the Amazon basin for a) NEP, b) GPP and c) TER.

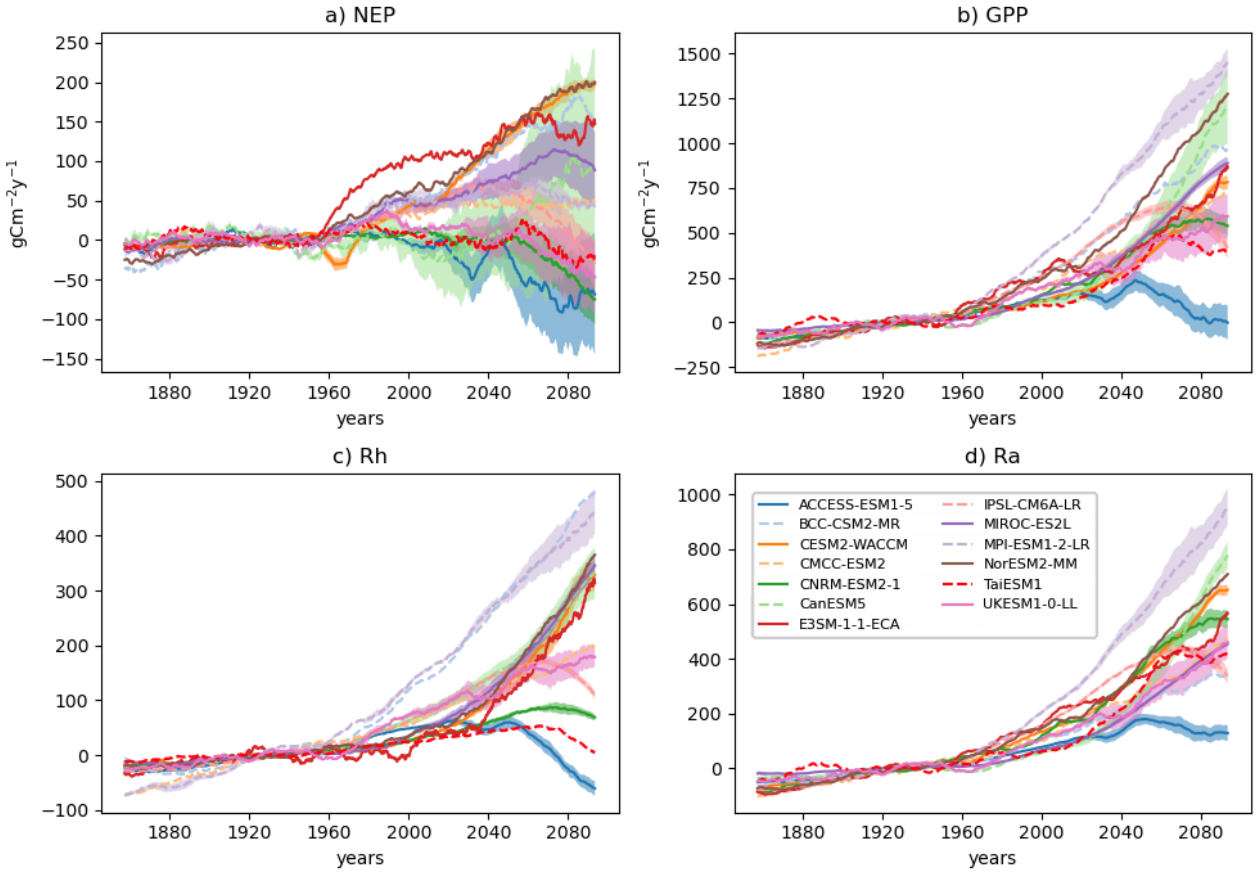

Figure S6: Simulated anomalies of (a) NEP, (b) GPP, (c) Rh and (d) Ra in the Amazon basin for the *hist* and *ssp585* experiments. Anomalies are computed with respect to the 1901-1960 mean. For the models with more than one realization, both the model-ensemble mean (line) and the spread (±1 standard deviation, shading) are shown. 4 years moving average values are shown for clarity.

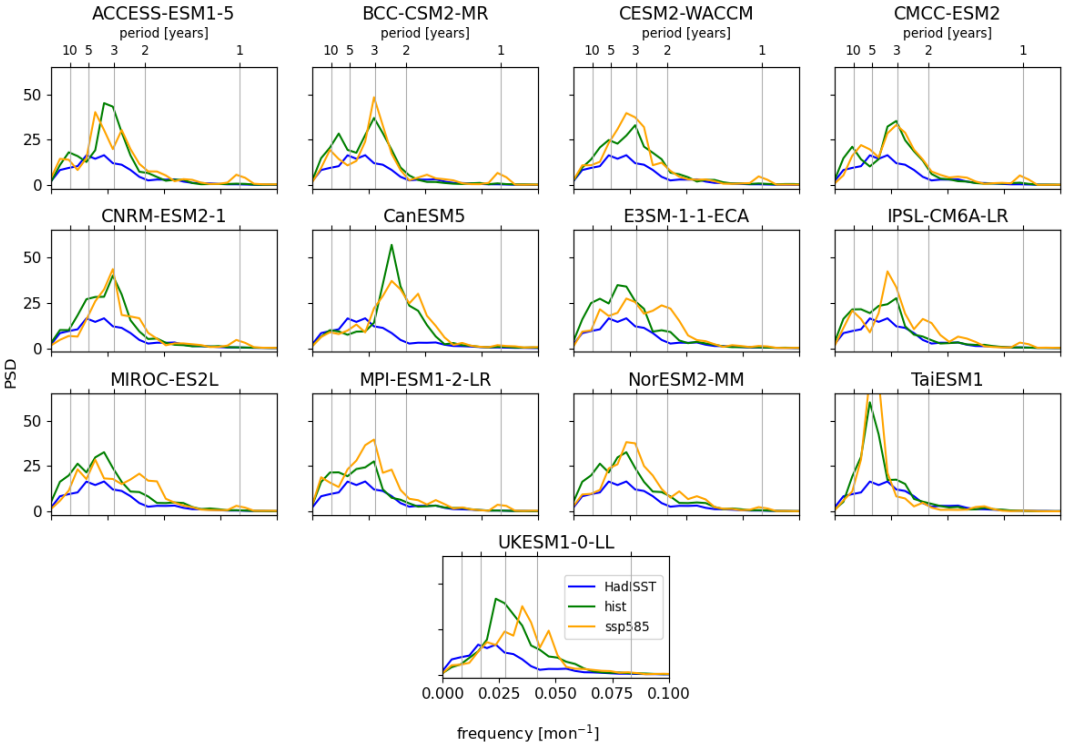

Figure S7: Power Spectrum Density (PSD) of the Nino3.4 signal in all the considered CMIP6 models under the historical (green) and ssp585 (yellow) scenarios. The historical HadISST Nino3.4 frequency (blue line) is added as reference.

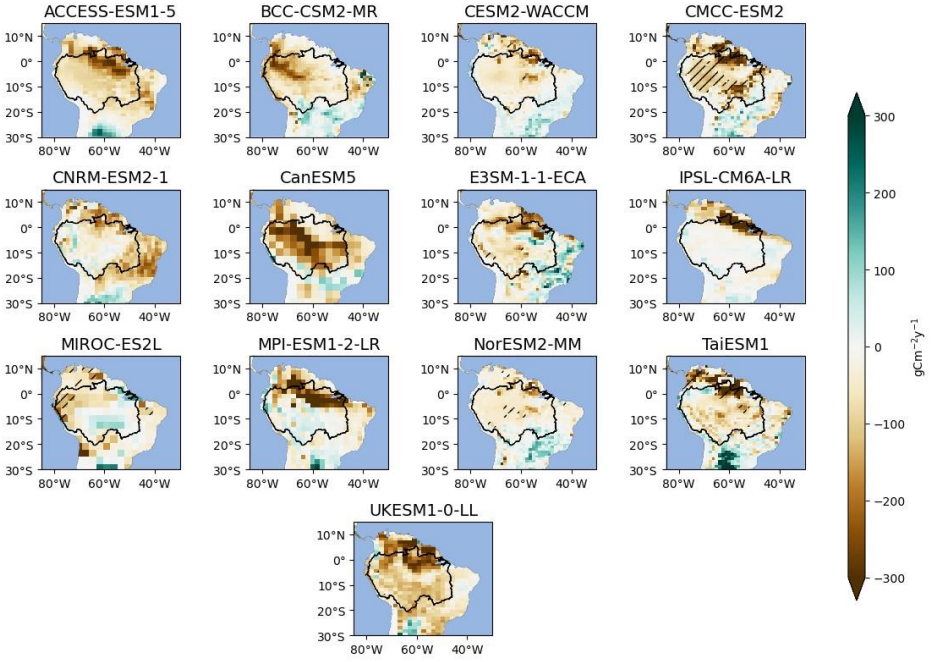

Figure S8: NEP response to El Nino during the historical period ($\boldsymbol{EN_{hist}}$). Hatches indicate statistically significant grid-cells according to a Mann-Whitney U-test. The Amazon basin, obtained from the SO HYBAM service (https://hybam.obs-mip.fr/), is also represented

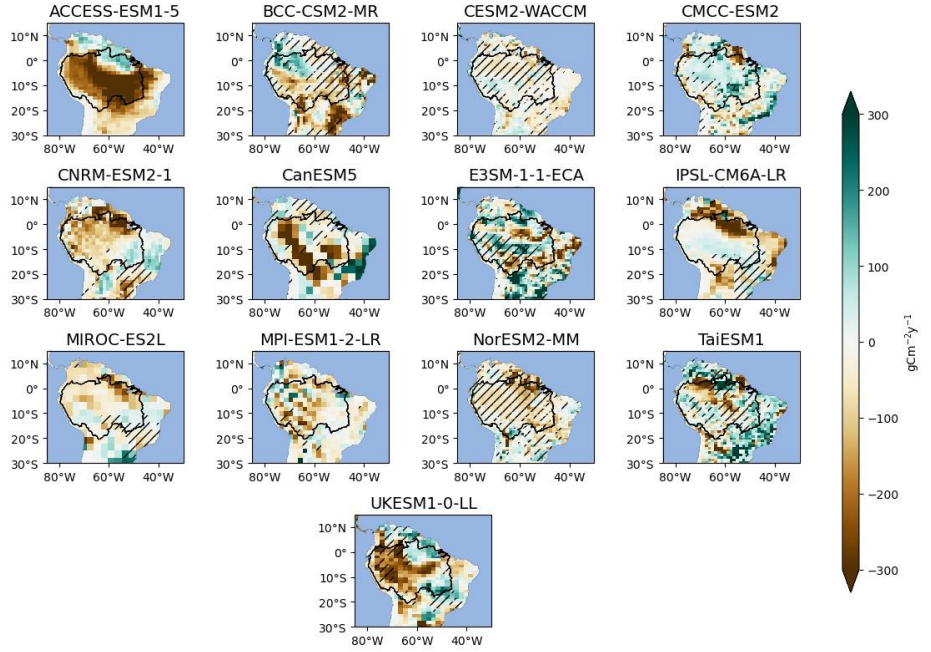

Figure S9: Difference in NEP response to El Nino composites in the ssp585 scenario compared to the historical (ΔEN). Hatches indicate statistically significant grid-cells according to a Mann-Whitney U-test. The Amazon basin, obtained from the SO HYBAM service (https://hybam.obs-mip.fr/), is also represented

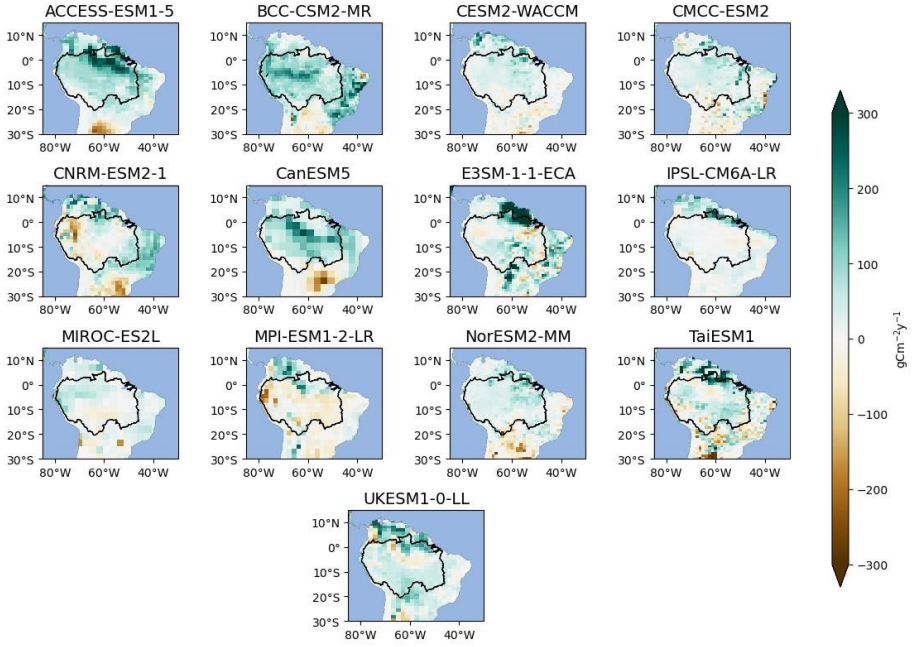

Figure S10: NEP response to La Nina composites in the historical scenario ($\boldsymbol{LN_{hist}}$). Hatches indicate statistically significant grid-cells according to a Mann-Whitney U-test. The Amazon basin, obtained from the SO HYBAM service (https://hybam.obs-mip.fr/), is also represented.

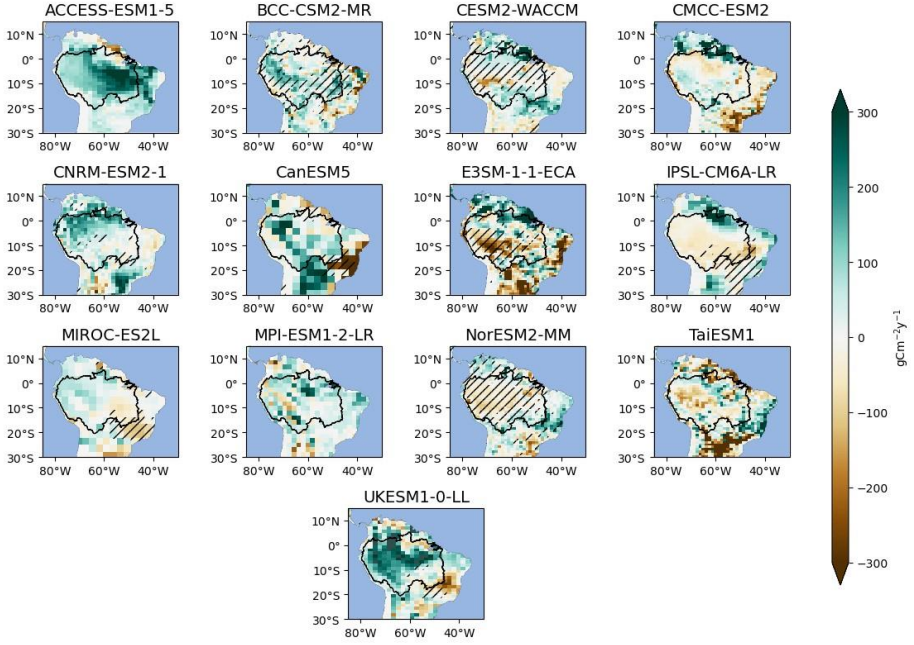

105

Figure S11: Difference in NEP response to La Nina composites in the ssp585 scenario compared to the historical (ΔLN). Hatches indicate statistically significant grid-cells according to a Mann-Whitney U-test. The Amazon basin, obtained from the SO HYBAM service (https://hybam.obs-mip.fr/), is also represented.

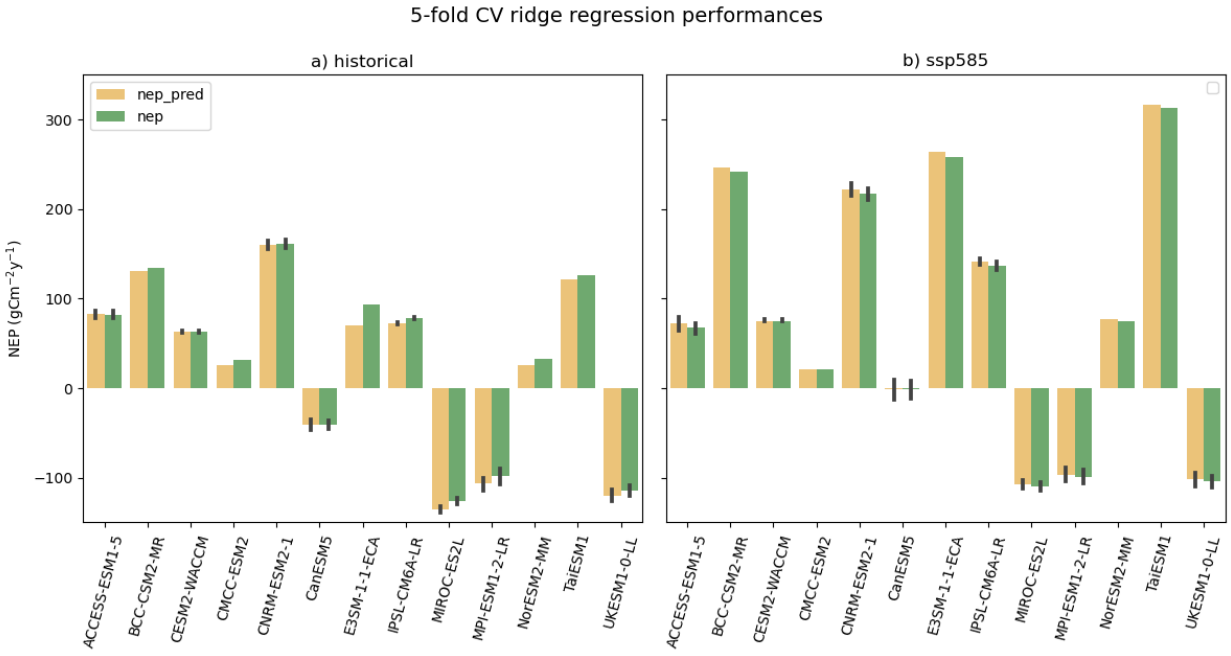

Figure S12: Regression model performance in the Amazon basin for a) historical and b) ssp585 scenarios. Differences among the zonal mean values of NEP predicted with the 5-CV ridge regression model (nep_pred) are reported as orange bars, while the zonal mean NEP directly retrieved from ESMs output (nep) are shown as green bars.

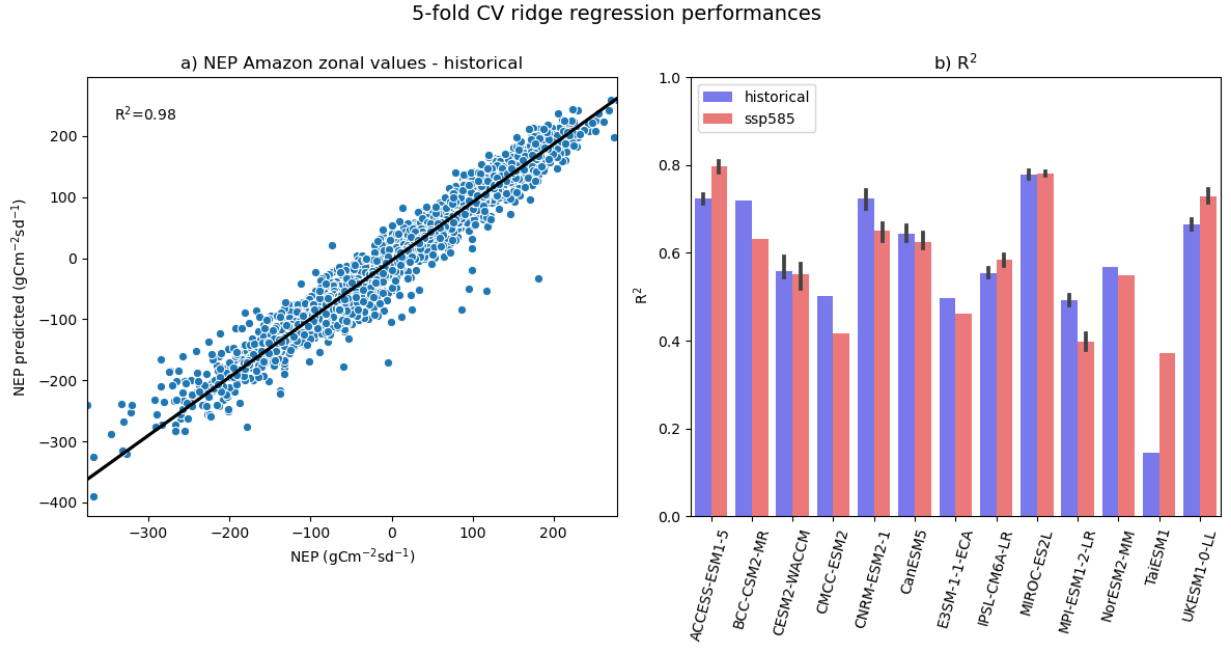

Figure S13: Regression model performance in the Amazon basin. a) Yearly DJF values of NEP predicted and NEP retrieved from ESMs. b) R2 values of the 5-fold CV ridge regression model, for both the historical and the ssp585 scenario.

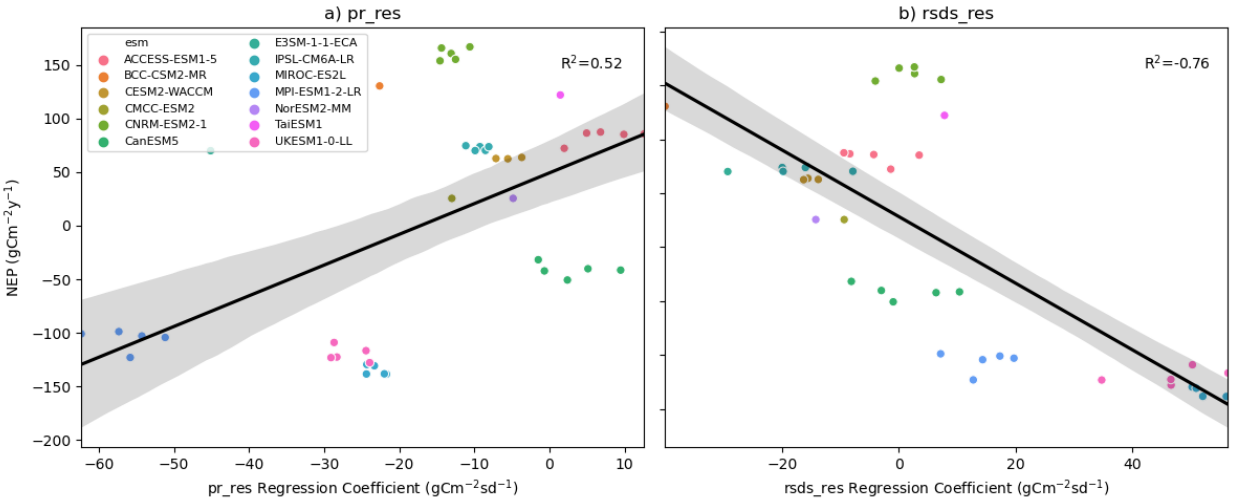

Figure S14: Model diversity in the representation of Amazon basin spatially averaged values for predicted NEP (on the y-axis), with respect to the regression coefficients of a) precipitation and b) shortwave incoming radiation, obtained with the MLR_iav regression. Shown are the values referring to the historical experiment. All the data have been detrended and standardized before the analysis.

120

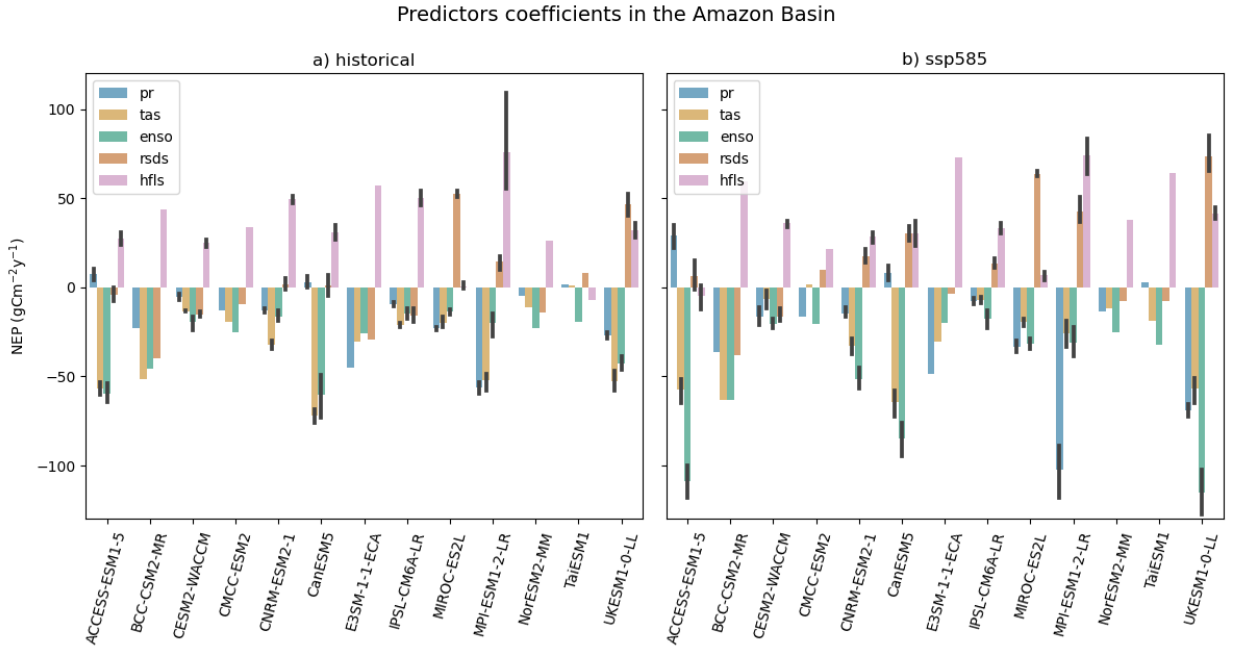

Figure S15: Values of zonal detrended 5-fold CV regression coefficients for the MLR_iav regression in the Amazon basin, for every ESM, for a) historical scenario and b) ssp585 scenario. The black vertical bars represent the spread in the predictors coefficients for models with more than one realization available.

125

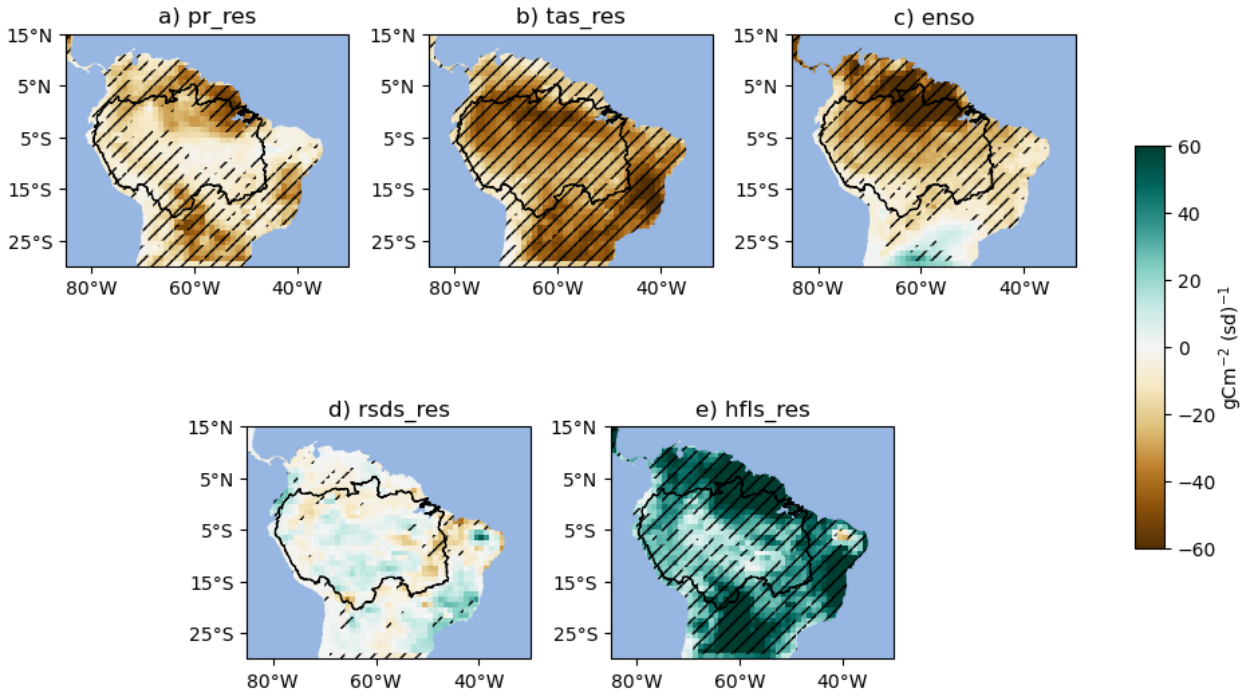

Figure S16: : Multi model ensemble mean of the coefficient values for the five climatic drivers obtained by the MLR_iav regression, for the ssp585 period. Hatches represent those grid cells for which at least 10 out of 13 ESM agree in the sign of the predictor value. The Amazon basin, obtained from the SO HYBAM service (https://hybam.obs-mip.fr/), is also represented.

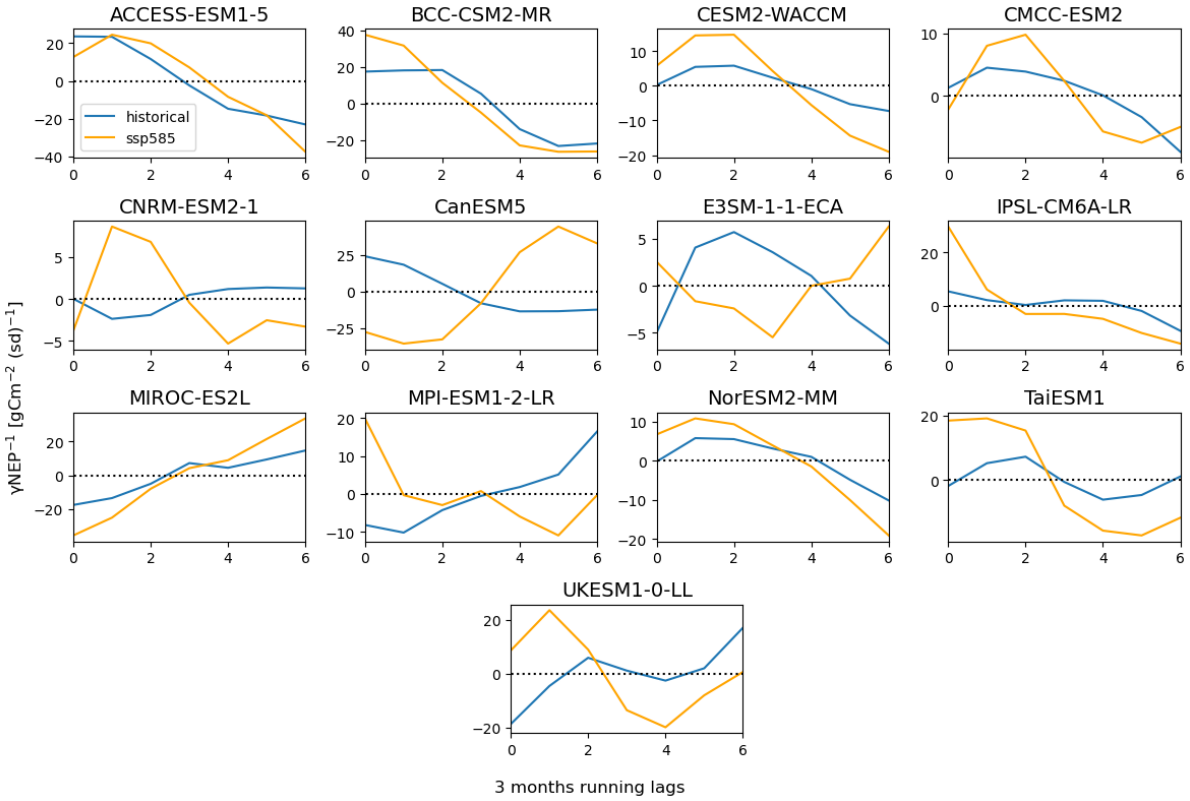

Figure S17: Time lagged ENSO teleconnection effect on Amazon basin NEP. Displayed are the value of the regression coefficient between the standardized Nino3.4 index in the DJF season, and the 3 months running zonal NEP mean in the Amazon basin. Please note that, on the y-axes, the inverse value of NEP regression coefficient is shown for clarity (higher values depict higher negative NEP anomalies).

Table S2: Regression coefficients and p-values of Tropical North Atlantic signal. The values represent the zonal mean effect on NEP in the Amazon basin, expressed in $\boldsymbol{gCm^{-2}y^{-1}}$, as also shown in Figure S17.

ESM	TNA coefficient - historical	TNA pvalue - historical	TNA coefficient – ssp585	TNA pvalue – ssp585
ACCESS-ESM1-5	-0.82	0.40	-7.27	0.43
BCC-CSM2-MR	-0.12	0.50	7.62	0.40
CESM2-WACCM	2.96	0.36	-0.53	0.43
CMCC-ESM2	0.64	0.48	4.81	0.38
CNRM-ESM2-1	2.32	0.44	-0.67	0.48
CanESM5	-1.00	0.44	5.06	0.43
E3SM-1-1-ECA	2.58	0.42	8.58	0.50
IPSL-CM6A-LR	0.17	0.45	-3.84	0.46
MIROC-ES2L	-3.00	0.41	-7.44	0.35
MPI-ESM1-2-LR	1.29	0.48	0.07	0.43
NorESM2-MM	-0.35	0.44	-0.58	0.51
TaiESM1	10.13	0.29	21.12	0.30
UKESM1-0-LL	-1.31	0.45	-1.69	0.48
Multimodel Mean	1.20	0.43	1.94	0.43

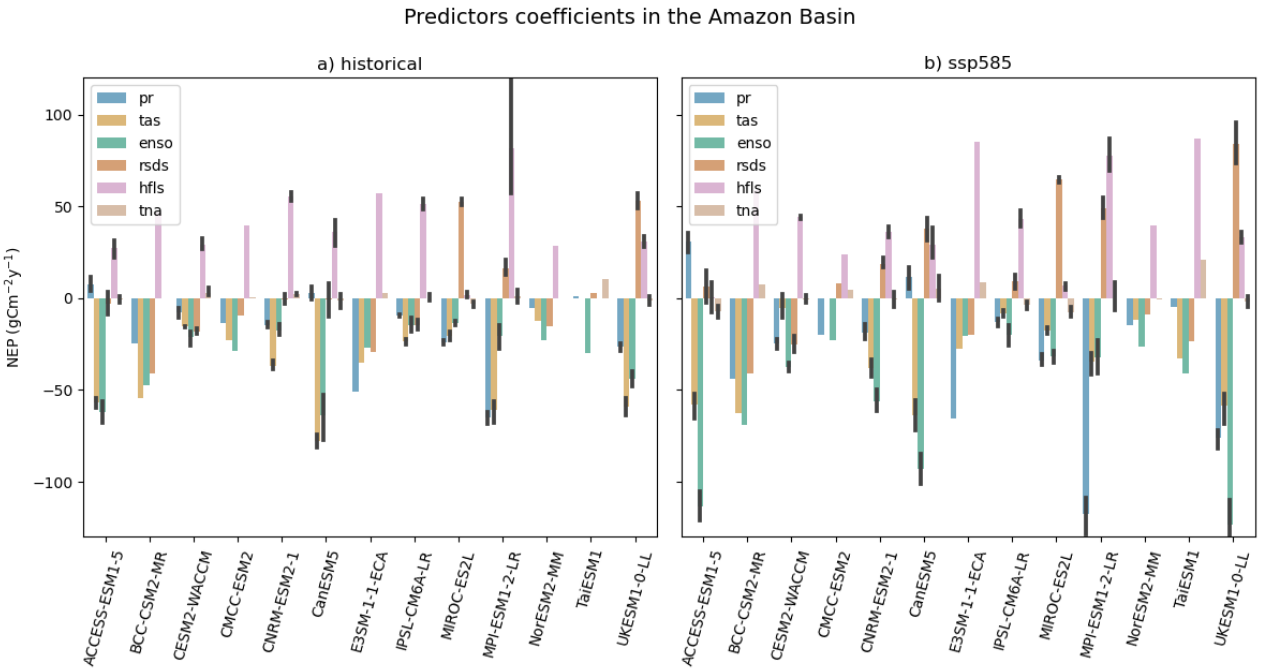

Figure S18: Multi model ensemble mean of the coefficient values of the drivers considered in the regression, for the ssp585 period. The black vertical bars represent the spread in the predictors coefficients for models with more than one realization available.

170

References

Boucher, O., Servonnat, J., Albright, A.L., Aumont, O., Balkanski, Y., Bastrikov, V., Bekki, S., Bonnet, R., Bony, S. and Bopp, L. (2020) 'Presentation and evaluation of the IPSL-CM6A-LR climate model', *Journal of Advances in Modeling Earth Systems*, 12(7), p. e2019MS002010.

Burrows, S.M., Maltrud, M., Yang, X., Zhu, Q., Jeffery, N., Shi, X., Ricciuto, D., Wang, S., Bisht, G. and Tang, J. (2020) 'The DOE E3SM v1. 1 biogeochemistry configuration: Description and simulated ecosystem-climate responses to historical changes in forcing', *Journal of Advances in Modeling Earth Systems*, 12(9), p. e2019MS001766.

Danabasoglu, G., Lamarque, J.-F., Bacmeister, J., Bailey, D.A., DuVivier, A.K., Edwards, J., Emmons, L.K., Fasullo, J., Garcia, R. and Gettelman, A. (2020) 'The community earth system model version 2 (CESM2)', *Journal of Advances in Modeling Earth Systems*, 12(2), p. e2019MS001916.

Hajima, T., Watanabe, M., Yamamoto, A., Tatebe, H., Noguchi, M.A., Abe, M., Ohgaito, R., Ito, A., Yamazaki, D. and Okajima, H. (2020) 'Development of the MIROC-ES2L Earth system model and the evaluation of biogeochemical processes and feedbacks', *Geoscientific Model Development*, 13(5), pp. 2197–2244.

Jung, M., Koirala, S., Weber, U., Ichii, K., Gans, F., Camps-Valls, G., Papale, D., Schwalm, C., Tramontana, G. and Reichstein, M. (2019) 'The FLUXCOM ensemble of global land-atmosphere energy fluxes', *Scientific data*, 6(1), pp. 1–14.

Jung, M., Schwalm, C., Migliavacca, M., Walther, S., Camps-Valls, G., Koirala, S., Anthoni, P., Besnard, S., Bodesheim, P., Carvalhais, N., Chevallier, F., Gans, F., Goll, D.S., Haverd, V., Köhler, P., Ichii, K., Jain, A.K., Liu, J., Lombardozzi, D., Nabel, J.E.M.S., Nelson, J.A., O'sullivan, M., Pallandt, M., Papale, D., Peters, W., Pongratz, J., Rödenbeck, C., Sitch, S., Tramontana, G., Walker, A., Weber, U. and Reichstein, M. (2020) 'Scaling carbon fluxes from eddy covariance sites to globe: synthesis and evaluation of the FLUXCOM approach', *Biogeosciences*, 17, pp. 1343–1365. Available at: https://doi.org/10.5194/bg-17-1343-2020.

Lovato, T., Peano, D., Butenschön, M., Materia, S., Iovino, D., Scoccimarro, E., Fogli, P.G., Cherchi, A., Bellucci, A. and Gualdi, S. (2022) 'CMIP6 Simulations With the CMCC Earth System Model (CMCC-ESM2)', *Journal of Advances in Modeling Earth Systems*, 14(3), p. e2021MS002814.

Mauritsen, T., Bader, J., Becker, T., Behrens, J., Bittner, M., Brokopf, R., Brovkin, V., Claussen, M., Crueger, T. and Esch, M. (2019) 'Developments in the MPI-M Earth System Model version 1.2 (MPI-ESM1. 2) and its response to increasing CO2', *Journal of Advances in Modeling Earth Systems*, 11(4), pp. 998–1038.

Monteverde, C., De Sales, F. and Jones, C. (2022) 'Evaluation of the CMIP6 Performance in Simulating Precipitation in the Amazon River Basin', *Climate*, 10(8), p. 122. Available at: https://doi.org/10.3390/cli10080122.

Ortega, G., Arias, P.A., Villegas, J.C., Marquet, P.A. and Nobre, P. (2021) 'Present-day and future climate over central and South America according to CMIP5/CMIP6 models', *International Journal of Climatology* [Preprint]. Available at: https://doi.org/10.1002/JOC.7221.

Qiao, L., Zuo, Z. and Xiao, D. (2022) 'Evaluation of Soil Moisture in CMIP6 Simulations', *Journal of Climate*, 35(2), pp. 779–800. Available at: https://doi.org/10.1175/JCLI-D-20-0827.1.

Rayner, N.A.A., Parker, D.E., Horton, E.B., Folland, C.K., Alexander, L.V., Rowell, D.P., Kent, E.C. and Kaplan, A. (2003) 'Global analyses of sea surface temperature, sea ice, and night marine air temperature since the late nineteenth century', *Journal of Geophysical Research: Atmospheres*, 108(D14).

Séférian, R., Nabat, P., Michou, M., Saint-Martin, D., Voldoire, A., Colin, J., Decharme, B., Delire, C., Berthet, S. and Chevallier, M. (2019) 'Evaluation of CNRM earth system model, CNRM-ESM2-1: Role of earth system processes in present-day and future climate', *Journal of Advances in Modeling Earth Systems*, 11(12), pp. 4182–4227.

Seland, Ø., Bentsen, M., Olivié, D., Toniazzo, T., Gjermundsen, A., Graff, L.S., Debernard, J.B., Gupta, A.K., He, Y.-C. and Kirkevåg, A. (2020) 'Overview of the Norwegian Earth System Model (NorESM2) and key climate response of CMIP6 DECK, historical, and scenario simulations', *Geoscientific Model Development*, 13(12), pp. 6165–6200.

Sellar, A.A., Jones, C.G., Mulcahy, J.P., Tang, Y., Yool, A., Wiltshire, A., O'connor, F.M., Stringer, M., Hill, R. and Palmieri, J. (2019) 'UKESM1: Description and evaluation of the UK Earth System Model', *Journal of Advances in Modeling Earth Systems*, 11(12), pp. 4513–4558.

Swart, N.C., Cole, J.N., Kharin, V.V., Lazare, M., Scinocca, J.F., Gillett, N.P., Anstey, J., Arora, V., Christian, J.R. and Hanna, S. (2019) 'The Canadian earth system model version 5 (CanESM5. 0.3)', *Geoscientific Model Development*, 12(11), pp. 4823–4873.

Wang, Y.-C., Hsu, H.-H., Chen, C.-A., Tseng, W.-L., Hsu, P.-C., Lin, C.-W., Chen, Y.-L., Jiang, L.-C., Lee, Y.-C., Liang, H.-C., Chang, W.-M., Lee, W.-L. and Shiu, C.-J. (2021) 'Performance of the Taiwan Earth System Model in Simulating Climate Variability Compared With Observations and CMIP6 Model Simulations', *Journal of Advances in Modeling Earth Systems*, 13(7), p. e2020MS002353. Available at: https://doi.org/10.1029/2020MS002353.

Wild, M., Folini, D., Hakuba, M.Z., Schär, C., Seneviratne, S.I., Kato, S., Rutan, D., Ammann, C., Wood, E.F. and König-Langlo, G. (2015) 'The energy balance over land and oceans: an assessment based on direct observations and CMIP5 climate models', *Climate Dynamics*, 44(11), pp. 3393–3429. Available at: https://doi.org/10.1007/s00382-014-2430-z.

Wu, T., Lu, Y., Fang, Y., Xin, X., Li, L., Li, W., Jie, W., Zhang, J., Liu, Y. and Zhang, L. (2019) 'The Beijing Climate Center climate system model (BCC-CSM): the main progress from CMIP5 to CMIP6', *Geoscientific Model Development*, 12(4), pp. 1573–1600.

Ziehn, T., Chamberlain, M.A., Law, R.M., Lenton, A., Bodman, R.W., Dix, M., Stevens, L., Wang, Y.-P. and Srbinovsky, J. (2020) 'The Australian earth system model: ACCESS-ESM1. 5', *Journal of Southern Hemisphere Earth Systems Science*, 70(1), pp. 193–214.